Weather and Climate Extremes 34 (2021) 100370

Contents lists available at ScienceDirect

Weather and Climate Extremes

journal homepage: www.elsevier.com/locate/wace

Characterization of the atmospheric environment during extreme precipitation events associated with atmospheric rivers in Norway - Seasonal and regional aspects

Clio Michel [a,*], Asgeir Sorteberg [a], Sabine Eckhardt [b], Chris Weijenborg [c], Andreas Stohl [d], Massimo Cassiani [b]

[a] Geophysical Institute, University of Bergen and Bjerknes Centre for Climate Research, Bergen, Norway
[b] Norwegian Institute for Air Research, Kjeller, Norway
[c] Meteorology and Air Quality Group, Wageningen University, Wageningen, The Netherlands
[d] Faculty of Earth Sciences, Geography and Astronomy, University of Vienna, Austria

ARTICLE INFO

Keywords:
Atmospheric rivers
Extreme precipitation events
Large-scale atmospheric circulation
Rossby wave breaking

ABSTRACT

Extreme precipitation events in Norway in all seasons are often linked to atmospheric rivers (AR). We show that during the period 1979–2018 78.5% of the daily extreme precipitation events in Southwestern Norway are linked to ARs, this percentage decreasing to 59% in the more northern coastal regions and ~40% in the inland regions. The association of extreme precipitation with AR occurs most often in fall for the coastal areas and in summer inland. All Norwegian regions experience stronger winds and 1–2°C increase of the temperature at 850 hPa during AR events compared to the climatology, the extreme precipitation largely contributing to the wet climatology (only considering rainy days) in Norway but also in Denmark and Sweden when the rest of Europe is dry. A cyclone is found nearby the AR landfall point in 70% of the cases. When the cyclone is located over the British Isles, as it is typically the case when ARs reach Southeastern Norway, it is associated with cyclonic Rossby wave breaking whereas when the ARs reach more northern regions, anticyclonic wave breaking occurs over Northern Europe. Cyclone-centered composites show that the mean sea level pressure is not significantly different between the eight Norwegian regions, that baroclinic interaction can still take place although the cyclone is close to its decay phase and that the maximum precipitation occurs ahead of the AR. Lagrangian air parcel tracking shows that moisture uptake mainly occurs over the North Atlantic for the coastal regions with an additional source over Europe for the more eastern and inland regions.

1. Introduction

Atmospheric rivers (AR) are transient elongated bands of large moisture fluxes that usually extend from the tropics to the higher latitudes (Newell et al., 1992) and can produce large amounts of precipitation along with strong winds when reaching land (Zhu and Newell, 1998; Ralph et al., 2004, 2006; Leung and Dian, 2009; Gimeno et al., 2016; Waliser and Guan, 2017) leading to floods, landslides, and wind storms (Stohl et al., 2008; Liberato et al., 2012; Trigo et al., 2014, Table 1 in Ralph et al., 2019). ARs are especially linked to extreme precipitation events when they impinge on regions with steep topography, enhancing the moisture ascent, such as the Western North American or Norwegian coasts in the Northern Hemisphere, although the direction at which the AR hits the topography can determine the extreme occurrence (Ralph et al., 2003; Neiman et al., 2011, 2013; Lavers and Villarini, 2013; Hughes et al., 2014; Hecht and Cordeira, 2017). For example, along southwestern Norway, which has an elevated and abrupt topography, almost all extreme precipitation events were associated with ARs (Azad and Sorteberg, 2017). The moisture is driven towards the topography because of a low-level jet associated with a strong sea level pressure (SLP) gradient between low pressure to the north and high pressure to the south (Ralph et al., 2004; Heikkilä and Sorteberg, 2012). Interestingly, already Bjerknes and Solberg (1921) realized the relationship between the orientation of a cyclone's cold front, the moisture flux, and the topography in southwestern Norway, long before ARs became a topic of research. Their results are still valid

* Corresponding author.
E-mail address: Clio.Michel@uib.no (C. Michel).

https://doi.org/10.1016/j.wace.2021.100370
Received 24 December 2020; Received in revised form 3 August 2021; Accepted 11 August 2021
Available online 13 August 2021

today and fully applicable to ARs impinging on a coastal mountain range. Studying the month of December 2006, Sodemann and Stohl (2013) showed that ARs' axis coincide with the upper-troposphere jet stream orientation, indicating a coupling to the large-scale atmospheric circulation, and that ARs can be associated with multiple cyclones with moisture uptake over ocean rather locally but also at southern latitudes. In this study, we focus on the extreme precipitation events occurring in Norway during all seasons of the last 40 years (1979–2018) using observations and an atmospheric reanalysis to emphasize some regional differences when other studies focused on specific regions, one season or even a few months (Sodemann and Stohl, 2013; Azad and Sorteberg, 2017; Benedict et al., 2019). We characterize ARs and the large-scale circulations linked to these extreme events with a focus on the cyclones themselves. This allows us to show with composites the two ways moisture is transported towards Norway found by Sodemann and Stohl (2013), linking ARs, Rossby wave breaking, jet, and cyclones. Finally, we determine the moisture sources during the extreme precipitation events associated with ARs in an attempt to generalize the previous results of Sodemann and Stohl (2013) and Stohl et al. (2008).

An example of extreme precipitation event associated with an AR hitting Norway is the weather system named *Loke*. It illustrates the features of ARs reaching Norway addressed in this study in a statistical way, such as the large-scale atmospheric circulation, the association with synoptic cyclones, anticyclones, and wave breaking when such an event occurs. *Loke* occurred in November 2005, gave extreme precipitation in many stations of southwestern Norway and triggered 139 landslides, among which 103 were debris slides, mudslides, and soil landslides, 21 were rock falls and 15 snow avalanches (see Fig. 6 of Bondevik and Aa, 2014). This extreme precipitation event was associated with an AR, which was first linked to an anticyclone over the North

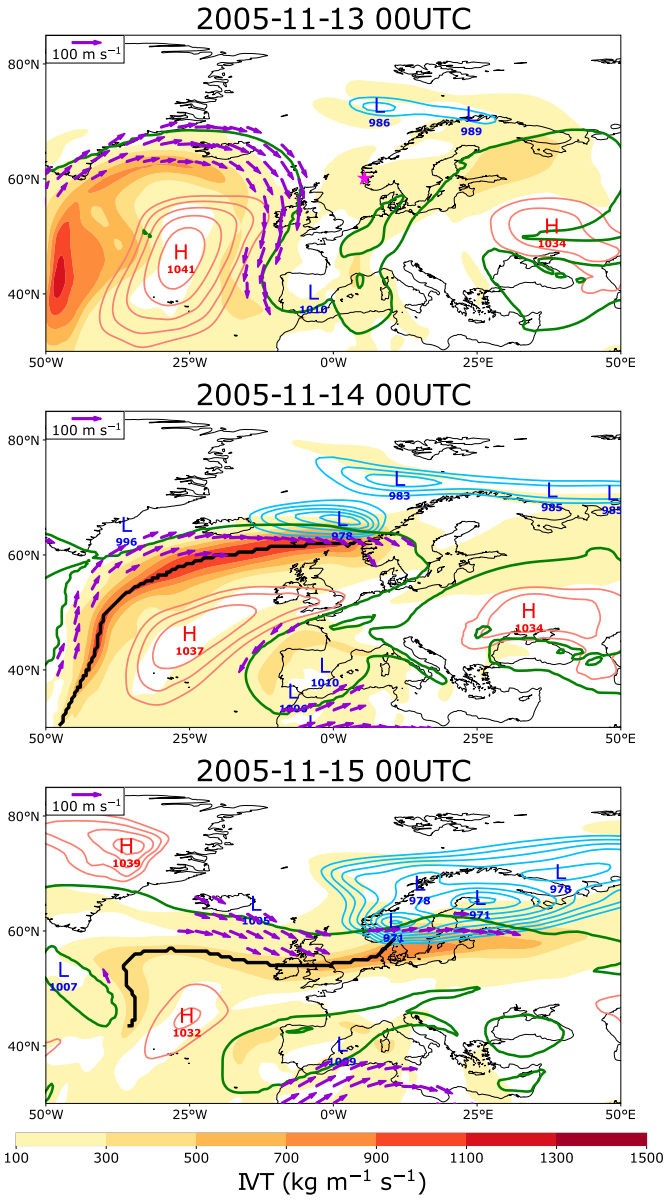

Fig. 1. Illustration of an AR hitting Norway and leading to extreme precipitation. Shown from 13 November 2005 00UTC to 15 November 2005 00UTC are the integrated water vapor transport (shading, unit: kg m^{-1} s^{-1}), cyclone mask (blue contours), 320-K isentrope on the 2-PVU surface (green contour), 250-hPa wind larger than 50 m s^{-1} (violet arrows) and mean sea level pressure (red contours from 1030 hPa upward and blue contours from 990 hPa downward with an interval of 2.5 hPa). The letters H and L mark the locations of the high and low pressure systems with their pressure value (in hPa) underneath. The small pink star in the top panel shows the location of Opstveit, the station with the highest precipitation during this event. The black line shows the AR as defined by the detection algorithm. (For interpretation of the references to color in this figure legend, the reader is referred to the Web version of this article.)

Atlantic creating a ridge around which the moisture winded itself from the west (13 November 00UTC in Fig. 1). When the anticyclone began to decay in intensity, a cyclone formed northwest of Iceland north of the upper-tropospheric jet and, while intensifying, propagated zonally towards Norway, already bringing large amounts of rain in southwestern Norway. The moisture plume feeding and created by the cyclone reached Norway as an AR for the first time on 14 November 00UTC, leading to a maximum of 223 mm of rain, measured between 06UTC on November 14 and 06UTC on November 15, in the station of Opstveit (in southern Norway of and close to the station of Indre Matre where the Norwegian all-time daily record of 229.6 mm was observed, see pink star in top panel of Fig. 1). The cyclone continued its path eastward over Norway and Sweden and the last time at which an AR was detected was 15 November 00UTC. We can also see that this event was associated with an anticyclonic reversal of the 320-K isentrope on the tropopause that is an anticyclonic wave breaking over Europe (green line in Fig. 1).

The large-scale atmospheric circulation affects the ARs' trajectory. For example, it has been shown that, in winter or fall, during the positive phase of the North Atlantic Oscillation (NAO+), the number of ARs reaching Norway increases due to the more southwest-northeastward direction of the jet stream whereas during negative phase of the NAO (NAO-), not many ARs reach Norway because of the southern position of the jet (Uvo, 2003; Hanssen-Bauer, 2005; Heikkilä and Sorteberg, 2012; Benedict et al., 2019). A more detailed description of the large-scale flow configuration promoting ARs towards Europe is given by Pasquier et al. (2018) using the decomposition in weather regimes considering all seasons together. They showed that southwestern Norway is located at the end of the climatological jet hence regularly hit by ARs especially during the Zonal (often associated with NAO+) and Atlantic Trough weather regimes. ARs reach Northern Norway when there is European Blocking. However, it is less likely for ARs to hit Norway when Greenland Anticyclone (often associated with NAO-) and Atlantic Ridge weather regimes occur. Their results are valid for all seasons and in accordance to the effects of the Atlantic blocking (that can be related to the Atlantic Ridge weather regime in Pasquier et al. (2018)) and European blocking as defined by Sousa et al. (2017).

Most ARs and their associated consequences (temperature increase, precipitation, and wind) are linked to cyclonic systems (Bao et al., 2006) even though they are not an integrated part of cyclones such as fronts or warm conveyor belts. To exist and determine their intensity, ARs usually need both a cyclone on their poleward side and an anticyclone on their equatorward side (Lavers and Villarini, 2013; Zhang et al., 2019 for the North Pacific, and Guo et al., 2020) that create a zone of large SLP gradient hence strong geostrophic wind in between. Azad and Sorteberg (2017) especially emphasized that an AR is more likely to lead to extreme precipitation when an anticyclone builds up to the south, hence strengthening the pressure gradient and the moisture transport. In the North Pacific, about 80% of the ARs reaching land are tied to cyclones when only 45% of the cyclones are linked to ARs (Zhang et al., 2019). The spatial elongation and intensity of ARs seem influenced by the succession of propagating cyclones for several days (cyclone clusters, e.g., Sodemann and Stohl, 2013) meaning that ARs are relatively stationary compared to a cyclone's propagation speed. Cyclone clusters help gathering moisture, which favors heavy precipitation events. When propagating over open water, the cyclone extracts moisture from the ocean that converges ahead of its cold front and feeds its warm conveyor belt (Ralph et al., 2005; Dacre et al., 2015, 2019). The subsequent latent heat release then contributes to intensify the cyclone, in particular when the AR associated with the cyclone has a strong intensity (Zhang et al., 2019). The topography-enhanced air mass lifting increases the impact of the AR leading to extreme precipitation. The AR's strength partly depends on the moisture availability which increases when the sea surface temperatures increase (Zavadoff and Kirtman, 2020). When linked to a cyclone, the arrival of an AR also means the arrival of the warm sector of a cyclone, hence increased temperatures. Therefore, in winter, ARs can lead to rain-on-snow events that increases the risk of flood (precipitation plus snow melt, Guan et al., 2016) and is problematic for the fauna (Putkonen and Roe, 2003).

Although ARs were originally thought to bring moisture from the tropics to the higher latitudes (see recent study by Ramos et al., 2016), most of them are now viewed as the footprint of a cyclone propagation over the ocean (Dacre et al., 2015). When ARs are associated with cyclones, the moisture uptake takes mostly place at local scale (Bao et al., 2006; Dacre et al., 2015, 2019; Sodemann and Stohl, 2013) whereas when they are associated with anticyclones (Zhang et al., 2019) and for stronger precipitation events (Stohl et al., 2008) the moisture source is rather located in the tropics. The location of the moisture uptake for the precipitation over Norway varies from season to season with uptake over land in summer and over ocean during the other seasons (Stohl et al., 2008). Knowing the origin of the moisture can help to understand climatic changes in Norway as these changes can potentially be associated with variations at the source location.

When reaching land on the eastern side of the oceanic basins, cyclones linked to ARs are usually close to their decay phase and can be associated with Rossby wave breaking (Hu et al., 2017; Zavadoff and Kirtman, 2020) although when the AR has a strong intensity, cyclones can still deepen (Zhang et al., 2019). The potential further deepening means that the cyclone can lead to even stronger impacts in terms of precipitation and wind. Rossby wave breaking events are the irreversible overturning of isentropes at the tropopause occurring at the end of the cyclone's life cycle that through the divergence and convergence of eddy momentum fluxes accelerates and decelerates the jet (eddy-driven jet). The wave breaking is called anticyclonic when the wave elongates along a southwest-northeast direction and is called cyclonic when the wave elongates from the southeast to the northwest. The effect of the wave breaking on the mean flow is a poleward (equatorward) displacement of the eddy-driven jet for an anticyclonic (cyclonic) wave breaking (McIntyre and Palmer, 1983; Thorncroft et al., 1993; Rivière, 2009). The position of the jet then controls the location of the AR. As expected, ARs associated with anticyclonic (cyclonic) wave breaking hit the northern (southern) part of the continental areas (Hu et al., 2017). Zavadoff and Kirtman (2020) found that 73% of the ARs reaching Europe are linked to anticyclonic wave breaking and only a few are associated with cyclonic wave breaking whereas Hu et al. (2017) found a smaller percentage (~67%) of ARs associated with the two types of wave breaking. Sodemann and Stohl (2013) showed that ARs reaching Norway can be linked to cyclonic wave breaking with a single cyclone involved and a zonal jet or to anticyclonic wave breaking with several cyclones close to each other involved and a more tilted jet along the meridional direction. Weijenborg and Spengler (2020) recently related cyclone clustering to the occurrence of ARs over the North Atlantic.

In the next section, we describe the data along with the methods used. Section 3 deals with the extreme precipitation events, their seasonality, and how they are associated with ARs. Section 4 shows how the extreme events associated with ARs are related to the large-scale flow, the cyclones propagating over the North Atlantic, and where the moisture comes from.

2. Data and methods

2.1. Data

We use the European Centre for Medium-range Weather Forecasts (ECMWF) ERA-Interim reanalyses from 1979 to 2018 with a 6-hourly time resolution and interpolated on a regular $0.5^\circ \times 0.5^\circ$ spatial grid (Dee et al., 2011). ARs are detected from the 6-hourly vertically integrated water vapor transport (*IVT*) fields calculated using 22 vertical pressure levels from 1000 to 200 hPa, with an interval of 25 hPa between 1000 hPa and 750 hPa and of 50 hPa above 750 hPa. The zonal (IVT_u) and meridional (IVT_v) components of *IVT* are obtained as follows:

$$IVT_u = \frac{1}{g}\int_{1000}^{200} qu\,dp,\ IVT_v = \frac{1}{g}\int_{1000}^{200} qv\,dp \quad (1)$$

where q is the specific humidity, u and v the zonal and meridional components of the wind, p the pressure, and $g = 9.80665$ m s^{-2} the gravity. The IVT intensity is then

$$IVT = \sqrt{IVT_u^2 + IVT_v^2} \quad (2)$$

Per definition, the IVT combines both the lower troposphere where the specific humidity is the largest but the wind relatively weak and the upper troposphere where the specific humidity is small but the wind strong. Over the North Atlantic, the IVT is minimum during the shoulder seasons (April and November in Fig. 2) and maximum in winter and summer (January and July in Fig. 2). In January, the vertically integrated water vapor (IWV) is rather weak and the relative maximum of IVT in winter is mainly due to the large vertically integrated wind (Fig. 2a and e). On the contrary, in July, the relative maximum of IVT is mainly due to the large IWV (warm air can contain more moisture) because the vertically integrated wind is much weaker (Fig. 2c and g). Moreover, the maximum of IVT tilted from North America to Scandinavia slightly shifts northward in summer probably due to the jet shift (Fig. 2). Note that the specific humidity and windspeed are vertically integrated over pressure as has been done for the IVT (Eq. (1)).

In order to define extreme precipitation events, we use the 99.5th percentile of the daily observations for the same period as ERA-Interim. Observations are made publicly available by the Norwegian Meteorological Institute.[1] To get continuous time series as long as possible, the data from stations closer than 4 km (a 2-km threshold only leads to fewer stations without changing the results) and whose height difference is lower than 100 m with at least a 2-year overlap are compared. We have tested various correction methods, but with such short overlapping periods there are only two main options: either ignore the differences, as they are usually very small, or do a simple multiplicative correction for all values. We opted for the latter. The shortest timeseries is then corrected with a multiplicative factor, which is the ratio of the two stations over their common time period. This bias correction was applied to 91 stations. Finally, we only keep stations that have data for at least 95% of the days in 1979–2018, which gives a total of 206 stations over Norway, represented with blue dots in Fig. 3. Using a comparative trend analysis of precipitation, Hanssen-Bauer and Førland (1998) divided Norway in 13 regions, which we reduced to 8 regions, as displayed in Fig. 3, by merging regions sharing similar characteristics. The eight regions have different seasonal cycles with the largest precipitation in fall and early winter along the western Norwegian coast, in summer in Middle and Northern Inland and in summer and early fall over South Eastern Norway (Fig. 3).

To have the longest possible daily mean precipitation for Europe, we use the ensemble mean of the E-OBS dataset (v22.0e)[2] interpolated on a $0.25^\circ \times 0.25^\circ$ regular grid over the same time period (1979–2018) as ERA-Interim and the observations over Norway (Haylock et al., 2008; Cornes et al., 2018). E-OBS relies on station observations, over an extended European domain, that are interpolated on a regular grid. The ensemble is created by varying all parameters involved in the interpolation process such as, e.g, the radius around each grid point in which the stations have to be included. This process is not perfect and errors can arise especially over mountainous areas where gauge observations are scarce (see e.g., Hofstra et al., 2009). We will make use of the precipitation fraction here defined as the precipitation (pr) relative to the wet climatology ($clim_w$, average over days with precipitation $\geq$0.1 mm/day are considered) divided by the wet climatology: ($pr - clim_w$)/$clim_w = pr/clim_w - 1$. This measure is unitless and never lower than −1. Negative (positive) values mean that the precipitation amount is lower (higher) than the average intensity on a wet day. Values of −1 (0) mean that the amount of precipitation is zero (equal to the wet climatology). A value of 1 means that the precipitation is twice the wet climatology. Similarly, a value of 2 means that the precipitation is equal to three times the wet climatology, etc …

2.2. Detection of atmospheric rivers

We use a method similar to Brands et al. (2017) who identified ARs as lines following the maximum IVT values on 6-hourly fields starting from a specific region (Outten, 2019). The first step consists in computing the IVT percentiles for each grid point and calendar month only considering the period 1979–2009 as in Brands et al. (2017). The second step is to create a line along the region where we want to identify landfalling ARs, here the Norwegian coast (see red line in Fig. 3). Contrary to Brands et al. (2017) who divided Norway in two regions (lines 6 and 7 in their Fig. 1), we suppose that only one AR reaches Norway at every time step. The third step looks for the maximum IVT along the line and checks if it is larger than the detection percentile ($P_d = 90$) for the corresponding month. Once this point is identified, the algorithm determines the direction of the incoming flow, looks for the maximum IVT in this direction and checks if the value exceeds the tracking percentile ($P_t = 75$). The algorithm repeats these last steps as long as it finds IVT values exceeding P_t. The resulting track is discarded if its length is smaller than 3000 km as in Brands et al. (2017). Using this set-up we detect 9167 timesteps with ARs touching Norway for the whole 40 years of ERA-Interim (58440 6-hourly timesteps), meaning that an AR reaches Norway 15.7% of the time. At each timestep an AR is detected, we create a mask of the AR by putting ones when the IVT exceeds its 75th percentile and zeros elsewhere. Fig. S1h shows how often the mask overlaps the coastlines. South Western Norway is the Norwegian region most frequently hit by ARs (almost 60% of the time). The ARs making landfall in Norway pass over the north of the British Isles and Denmark, potentially impacting those areas as well. Note that only the timesteps at which ARs reach Norway are considered here but that some other features with high IVT can be detected at the same time, hence the non-zero percentages elsewhere.

The number of ARs detected is larger in winter and fall than in summer (Figs. S1a–e), which is in agreement with previous studies (Gao et al., 2016; Ralph et al., 2019). However, the choice of the percentiles and minimum length is rather subjective and affects the number of ARs detected (see e.g., Brands et al., 2017) and their seasonal cycle (Figs. S1a–e). The number of ARs increases when the detection and tracking percentiles decrease (n_{AR} in Figs. S1a–b,d-e) and when the minimum length is lower (Fig. S1c). The fraction of ARs (obtained by dividing the monthly numbers of ARs by the total of ARs detected) tends to increase in winter and decrease in summer when Pt decreases with Pd held constant (Figs. S1a and d), and to a lesser extent when Pd decreases with Pt held constant (Figs. S1b and e).

The seasonal cycle is different whether we consider all timesteps at which ARs are detected or only the number of events. In this sensitivity analysis, an event is defined when an AR lasts more than one timestep and is separated by at least 12h from another AR. Compared to AR timesteps, AR events are slightly more spread throughout the year (Fig. S1f) because AR events last longer in winter than summer although the duration difference is not significant (Fig. S1g). In the rest of the paper, we do not take into account whether an AR lasts for one or several timesteps.

2.3. Cyclone detection, masks, clusters, and rossby wave breaking

We use the cyclone detection and tracking algorithm of the Melbourne University (Murray and Simmonds, 1991) applied to the ERA-Interim 6-hourly mean sea level pressure (MSLP) field. The

[1] Data can be downloaded at: http://eklima.no.

[2] Publicly available at: https://surfobs.climate.copernicus.eu/dataaccess/access_eobs.php.

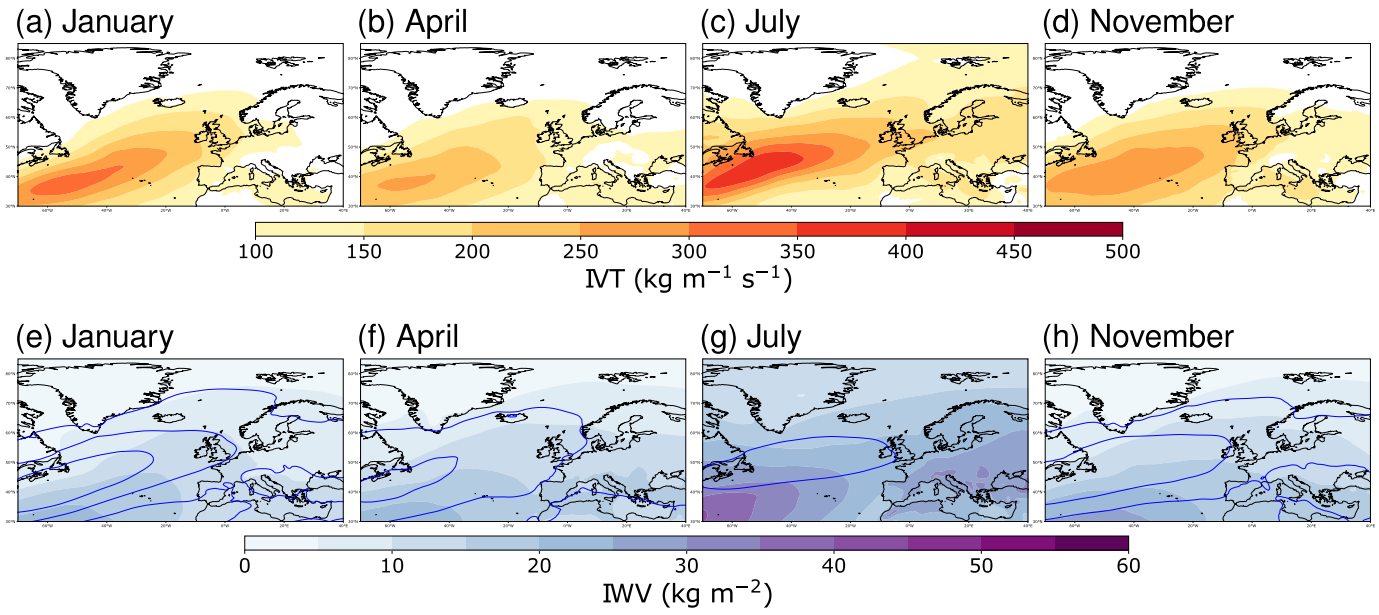

Fig. 2. (Top row) Climatology of IVT for the months of (a) January, (b) April, (c) July and (d) November. (bottom row) Climatology of IWV (shading) and vertically-integrated windspeed (blue contours starting from 120 10^3 kg m^{-1} s^{-1} with an interval of 40 10^3 kg m^{-1} s^{-1}) for the months of (e) January, (f) April, (g) July and (h) November. (For interpretation of the references to color in this figure legend, the reader is referred to the Web version of this article.)

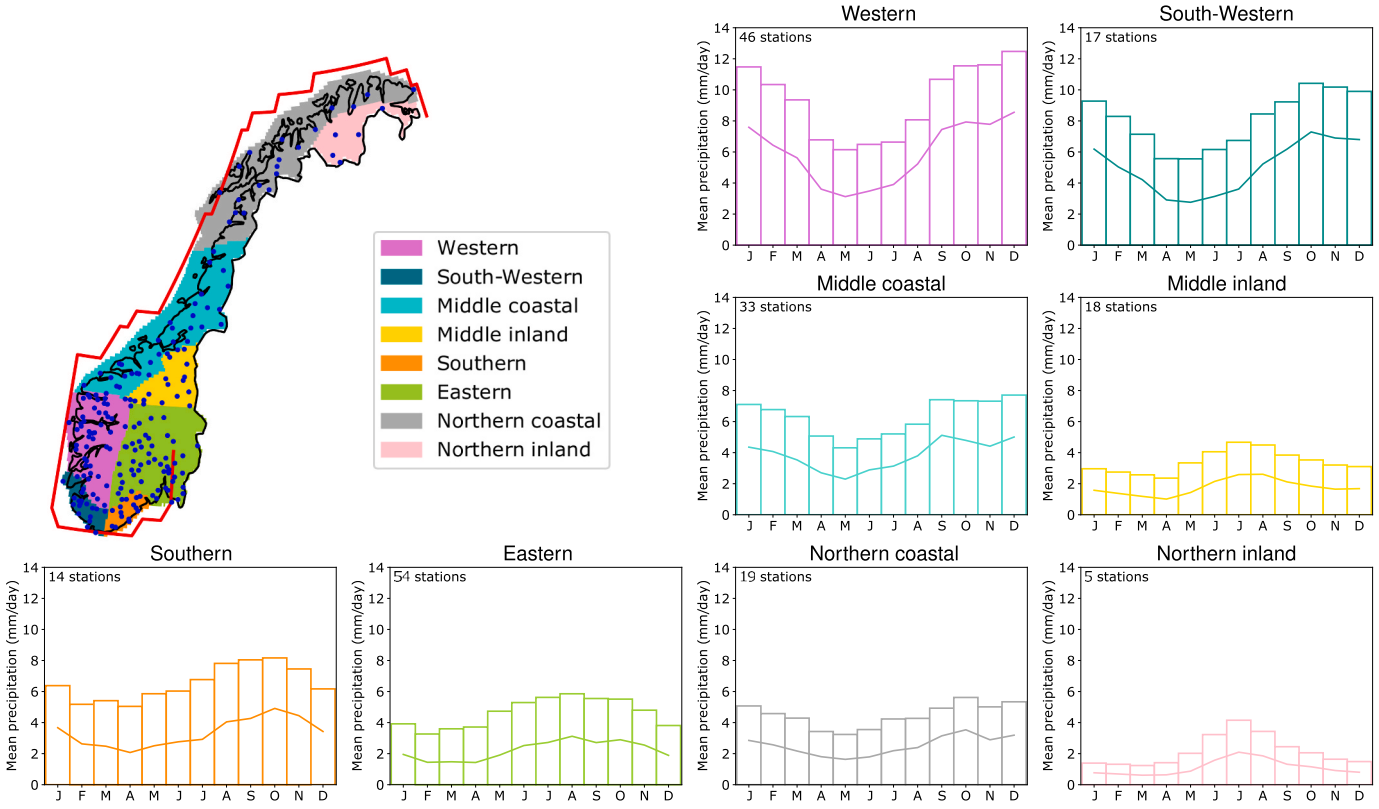

Fig. 3. Map displaying Norway divided in eight regions (colors) with the 206 stations used in this study superimposed (blue dots). The red line represents all possible starting points of the ARs detected. The different panels show the seasonal cycle of the mean precipitation in each region (for 1979–2018), the colors corresponding to the different regions. The bars display the wet-day climatology (only days with rainfall $\geq$0.1 mm are considered) and the lines the standard climatology (all days are considered). The number of stations in each region is given on the top left corner of each panel. (For interpretation of the references to color in this figure legend, the reader is referred to the Web version of this article.)

algorithm detects maxima in the Laplacian of MSLP and tracks them using a nearest-neighbour method. The namelists used here are the same as in Tsopouridis et al. (2020). Only cyclones with a life time of at least 24h are retained. A disc of radius R is defined around each cyclone to obtain a cyclone mask. R is here chosen to be the Rossby radius of deformation $R = (NH)/(\pi f)$ where N is the Brunt-Väisälä frequency, here held constant and equal to 1.3 10^{-2} s^{-1}, H is the scale height equal to 10 km, and f is the Coriolis parameter taken at the latitude of the

cyclone.

Cyclones clustering refer to the rapid temporal succession of cyclones over a given location. Bjerknes and Solberg (1922) described a type of cyclones cluster where there is a first cyclone ahead of secondary cyclones formed in its wake. However, there are other types of clusters and several methods to define them Dacre and Pinto (2020). Here we choose a method similar to Bevacqua et al. (2020). A grid point is defined as clustered if at least 3 cyclones pass this grid point within a radius R, as defined above (here using the grid point latitude to calculate f), with a maximum elapsed time of 2.5 days between each other. This gives a binary field for every time step. Compositing this field over the dates of extreme events associated with ARs highlight the frequency of clustered cyclones as a map.

Rossby wave breaking (RWB) is detected, using the method of Rivière (2009) and Michel and Rivière (2011), on low-resolution (4.5° × 4.5° spatial grid) daily potential vorticity fields at four different isentropic levels (300, 315, 330 and 350 K) to capture the tropopause at the different latitudes (Martius et al., 2007). The distinction is made between cyclonic and anticyclonic wave breakings. The four isentropic levels are averaged before compositing over the times of extreme events associated with ARs.

2.4. Identification of moisture sources

The origin of the extreme precipitation associated with ARs is investigated utilizing the Lagrangian Particle Transport model FLEXPART v10.4 (Pisso et al., 2019) following the method of Stohl and James (2004) for the moisture diagnostics. The model was driven with the 3-hourly ERA-Interim wind components, specific humidity, and precipitation data, obtained using the analysis times (00, 06, 12, and 18UTC) and the 3-h forecast starting at the analysis times (03, 09, 15, and 21UTC), from 1989 to 2018 interpolated on a 1° × 1° spatial grid. For each starting location, 50000 particles of equal mass distributed along the atmospheric vertical column above a 1° × 1° grid cell around the station location were released within ±3 h around the starting time and tracked backward for 12 days. To ensure that only particles contributing to precipitation are accounted for, the hourly average precipitation during the release had to be over 0.5 mm and the individual particles must have had a decrease in humidity, leading to precipitation upon arrival. The other particles are discarded. Specific humidity is conserved within one particle trajectory unless condensation or evaporation occurs leading to decrease or increase of specific humidity, respectively. Along every trajectory, the specific humidity is interpolated from ERA-Interim which provides the temporal change in specific humidity, which is equivalent to the evaporation-precipitation difference (E-P). In order to avoid the moisture uptake signal to be offset by the precipitation close to the extreme event region, we choose to only composite the trajectories segments that are within the planetary boundary layer whose height is calculated within FLEXPART. Between 1989 and 2018, there are 22108 starting locations and times corresponding to all stations experiencing an extreme precipitation event associated with an AR. As it is computationally expensive, we here track moisture sources for 29% of the cases, randomly chosen among the 22108 but approximately equally spread over the eight regions, resulting in 6408 starting times and locations.

3. Extreme precipitation events in Norway

Extreme daily precipitation is defined as the 99.5th percentile of the observed daily precipitation at every station over the whole period 1979–2018 (Fig. 4b) thus giving the same probability of extreme events at all stations. The most intense extreme events occur naturally, as a consequence of orographic enhancement, over the climatologically wettest part of Norway that is the southwestern coast. At each station, the 99.5th percentile is significantly correlated with the mean wet daily precipitation (Pearson correlation of 0.98) and they are both largest along the south-western coast of Norway (Fig. 4a and b). Averaged values for each region are given in Table 1. The season during which

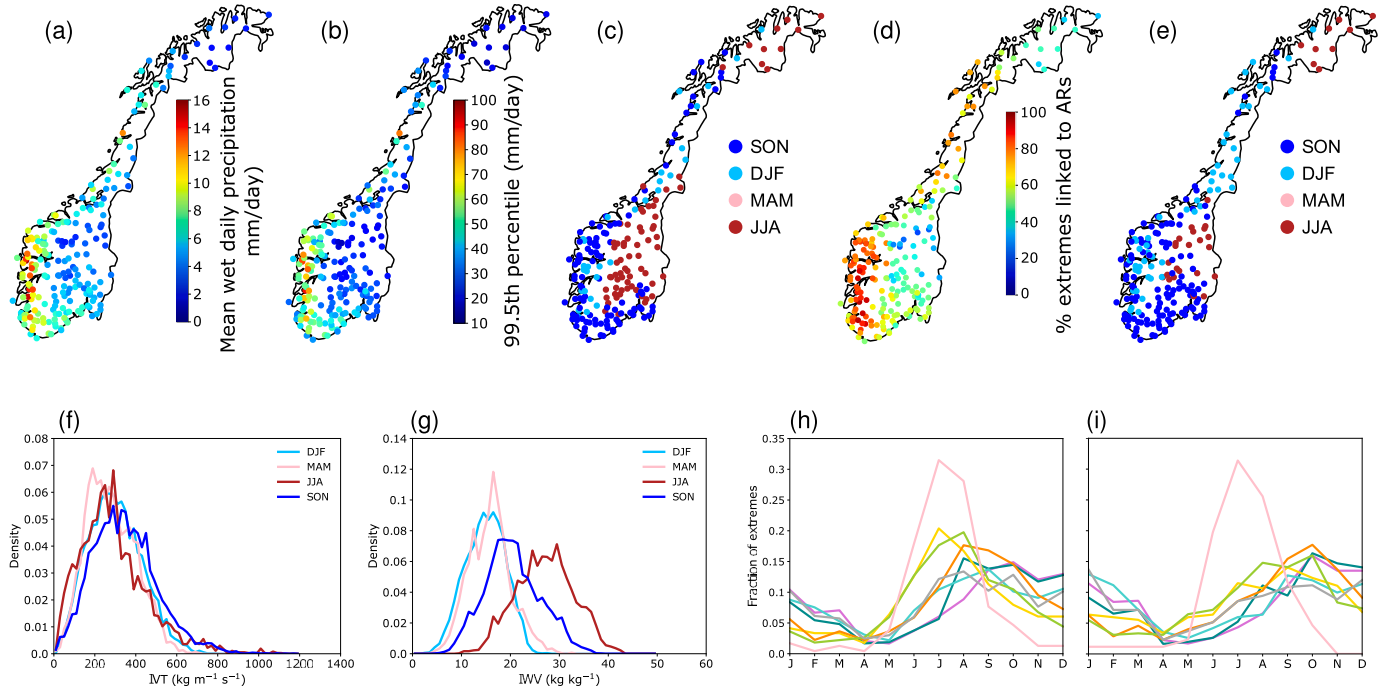

Fig. 4. For every selected station are displayed the (a) observed mean wet daily precipitation (in mm day^{-1}), (b) 99.5th percentile of the observed daily precipitation (in mm day^{-1}), (c) season in which most of the extreme events happen, (d) percentage of extreme precipitation events linked to ARs, (e) season at which most of the extreme events associated with ARs occur. (f) Normalized distributions of IVT for all extreme precipitation at all stations depending on the season (one color per season), (g) same as (f) but for IWV. Seasonal cycle of occurrence of (h) all extreme precipitation events and (i) extreme precipitation associated with ARs for each region separately (one color per region as defined in Fig. 3).

Table 1
Statistics for each region defined in Fig. 3 and for the period 1979–2018. The mean wet daily precipitation (MWDP) in mm, the 99.5th percentile of the daily precipitation in mm, the total number (unique days) and the mean number per year of extreme events and the fraction of extreme events occurring per season are displayed in the different columns from left to right. The abbreviations for the regions in the first column refer to: W: Western, SW: South Western, MC: Middle Coastal, MI: Middle Inland, S: Southern, E: Eastern, NC: Northern Coastal, and NI: Northern Inland regions.

Region	MWDP	99.5th perc.	Nb. extremes	Mean nb.	Fraction extreme			
			indiv. days	per year	DJF	MAM	JJA	SON
W	9.49	55.06	779	19.5	0.30	0.11	0.18	0.41
SW	8.26	47.63	477	11.9	0.27	0.08	0.25	0.40
MC	6.32	38.51	968	24.2	0.27	0.10	0.30	0.33
MI	3.47	22.09	628	15.7	0.14	0.11	0.50	0.25
S	6.62	42.68	357	8.9	0.15	0.10	0.34	0.41
E	4.71	28.67	992	24.8	0.10	0.11	0.50	0.29
NC	4.52	27.20	732	18.3	0.27	0.11	0.32	0.30
NI	2.16	17.54	235	5.9	0.03	0.06	0.77	0.14

most extreme precipitation events occur depends on the region. More inland regions such as Eastern, Middle and Northern Inland regions have their extreme precipitation occurring mostly in summer whereas the coastal regions experience their extreme precipitation in fall or winter (Fig. 4c,h and Table 1). The Middle Coastal and Eastern regions exhibit the highest numbers of unique extreme events and mean number per year (Table 1), which suggests that, in addition to the influence of the stations' density on this result, these events happen rather locally and not affect many stations at the same time within one region.

3.1. Association between daily extreme precipitation events and atmospheric rivers

We link daily extreme events to ARs when the AR occurs at any of the four timesteps covering the day of the event and the IVT at the grid point closest to the station exceeds the value of 100 kg m^{-1} s^{-1}. As the AR detection algorithm defines the AR axis with the starting point along the red line (Fig. 3), that is outside Norway, we need to use this subjectively-chosen IVT threshold to associate the AR with any station in Norway. A sensitivity analysis of the percentage of association extreme precipitation event/AR to the threshold (Fig. S2) showed that a value of 100 gave similar percentages as other previous studies (Azad and Sorteberg, 2017; Whan et al., 2020). A histogram of the IVT values for all stations at all timesteps of extreme events do not show difference with season contrary to the vertically-integrated specific humidity (Fig. 4f and g). Therefore, the use of an IVT threshold seems more appropriate. In agreement with Benedict et al. (2019), we find that most of the extreme events occurring along the western coast of Norway are associated with ARs although our percentage is smaller (~78.5% against 85% for Benedict et al., 2019) (see Fig. 4d and regions W, SW, S in Table 2), probably because of our different definitions of ARs and extremes. Over Southeastern Norway, the percentage decreases when going northward (Fig. 4d and regions S, E, MI in Table 2). One part of the reason may be because it is far from the coast and the association criterion is not fulfilled. A second part may be because the extremes can be associated with other atmospheric conditions (such as convection) since ARs and extreme events do not occur during the same seasons (fall/winter for ARs and rather summer for the extreme events). In the Middle and Northern Coastal regions, 59% of the extremes are linked to ARs and this percentage decreases when moving inland with 37 and 39% for Middle and Northern Inland regions, respectively (Table 2). When associated with ARs, the season with most frequent extreme events shifts towards the fall and winter months (Lavers and Villarini, 2013) as they are the months with largest AR frequency (compare Fig. 4c and e, Table 2). This is also visible when looking at the seasonal cycles of the extreme events frequency. The curves maximum clearly shifts towards fall and winter (compare Fig. 4h and i). For the Northern Inland region, most extremes associated with AR still occur mostly during summer.

The extreme precipitation distributions for events associated with ARs are not obviously different from the distributions for events not associated with ARs. The precipitation means and 90th percentiles are slightly larger (smaller) when the extremes are (not) associated with ARs than when all extremes are considered (except for the 90th percentile of Northern Inland, Table 2). The season in which the events occur also shifts from DJF along the coast to SON and JJA inland. In three out of the eight regions, the observed maximum extreme precipitation is not associated with an AR (Table 2). In two of these regions, most extremes occur in summer (Eastern and Northern Inland) suggesting that the maximum extreme may be linked to severe convection associated with thunderstorms (see e.g., Lavers and Villarini, 2013). Figure S3 shows an increase of convective available potential energy (CAPE) of ~80–100 J kg^{-1} for extreme precipitation events associated with ARs in all Norwegian regions meaning that there could be convective enhancement of precipitation. However, the CAPE anomaly is only significant for

Table 2
Statistics on the extreme precipitation events for each region as defined in Fig. 3 and for the period 1979–2018. (From left to right) Displayed are the region, the percentage of extreme events associated with ARs and the season when this link occurs most often in parenthesis, the mean and 90th percentile of the extreme precipitation for all extreme events (All), the extreme events associated (AR) and not associated (no AR) with ARs (in mm), and if the station's maximum extreme observed is linked or not linked to an AR (Yes/No) with the value of the maximum in parenthesis in mm. Abbreviations for the regions refer to: W: Western, SW: South Western, MC: Middle Coastal, MI: Middle Inland, S: Southern, E: Eastern, NC: Northern Coastal, and NI: Northern Inland regions.

Region	%extr. with ARs (season)	Mean precip./90th perc.			Max. precip.with ARs
		All	AR	no AR	
W	82% (SON)	68.19/99.7	69.67/101.76	61.47/90.65	Yes (223 mm)
SW	75% (SON)	60.07/85.3	62.34/88.4	53.27/75.48	Yes (163.4 mm)
MC	59% (DJF)	48.94/74.42	51.50/80.40	45.22/64.8	Yes (182.3 mm)
MI	37% (SON)	29.41/41.95	31.06/45.00	28.46/39.01	Yes (111.5 mm)
S	61% (SON)	54.49/73.66	55.20/75.45	53.41/69.54	No (154 mm)
E	48% (SON)	36.73/50.50	36.98/50.60	36.50/50.40	No (117.8 mm)
NC	59% (DJF)	35.25/52.30	37.94/55.21	31.26/47.00	Yes (105.5 mm)
NI	39% (JJA)	24.13/32.44	24.51/32.35	23.88/32.34	No (53.3 mm)

Northern Inland.

3.2. Link between daily extreme precipitation and IVT

The extreme precipitation amount is not linearly linked to IVT (Fig. 5a) and to IWV (not shown), which are both taken at the closest grid point to the station. One may think that the larger IVT the larger the precipitation but that is not really what is seen here. Therefore, it seems that the local conditions are important to determine the rainfall. For example, Hu et al. (2017) showed for the North Pacific that the transformation of water vapor into precipitation depends on the angle at which the AR hits the topography of the U.S. West Coast and is most efficient when the flow is more perpendicular to the mountain chain. For Norway, the flow direction towards the coastal mountain ranges has been identified already by Bjerknes and Solberg (1921) as a critical factor determining the intensity of precipitation during the passage of cyclones. This relationship is strengthened by a cold front forcing the air to rise over the mountains. In our study, the origin of the AR is obtained using the zonal and meridional components of the IVT (Eq. (1)). For Norway, the AR direction that gives the largest mean extreme precipitation depends on the region impacted (Fig. 5b). For Western Norway, 45% of the ARs associated with extreme precipitation come from the south-west direction and about 33% come from the west. The topography along the coast of the Western region is south-north oriented (see Fig. 1b of Benedict et al., 2019) which renders ARs from the west more efficient at triggering extreme precipitation than ARs from the south-west (see dark pink line on Fig. 5c) in accordance to Hu et al. (2017)'s results for the U.S. West Coast. For the South Western region, ARs from the south and southwest are most frequent but ARs from the west lead to a larger mean extreme precipitation (see dark cyan line on Fig. 5b and c). For the Southern and Eastern regions, ARs direction is most frequent from the south but the largest mean precipitation corresponds to the southeast direction (orange and green lines on Fig. 5b and c). For the Middle and Northern Inland regions, the mean extreme precipitation does not seem to depend on the IVT direction (yellow and light pink lines on Fig. 5b and c). For the Middle Coastal region, the most frequent IVT direction is from the west and is associated with the largest mean extreme precipitation (light blue line on Fig. 5b and c). Finally, for the Northern Coastal region, the most frequent IVT direction is from the west and southwest with the largest mean extreme precipitation for both of these directions (gray line on Fig. 5b and c).

4. Atmospheric rivers' characteristics and large-scale flow

In the following, we create composites over the timesteps of the ARs that have been linked to extreme precipitation events, the number of

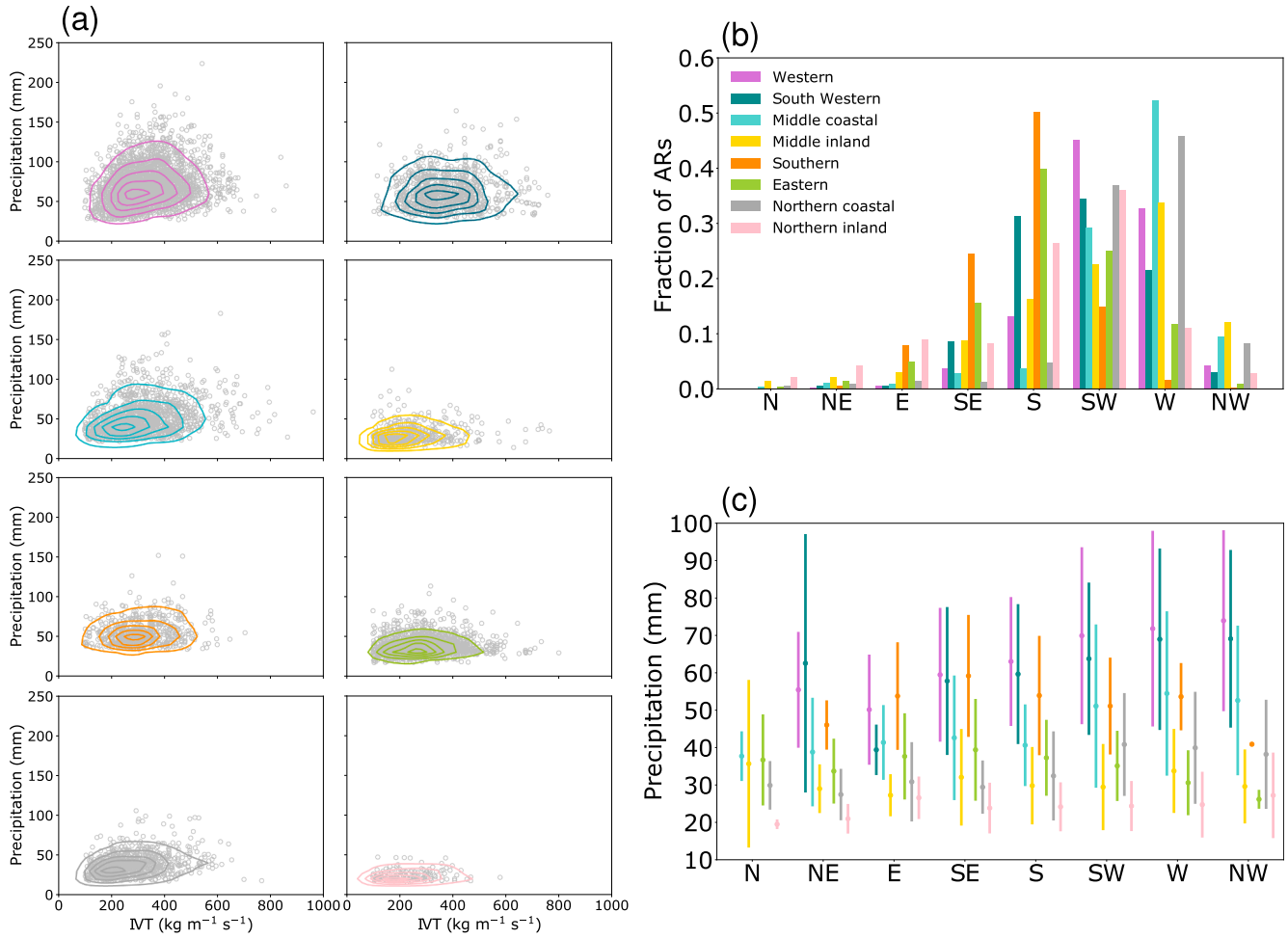

Fig. 5. (a) Extreme precipitation as a function of the integrated water vapor transport (IVT) for all events associated with ARs (gray dots) and all regions in the eight panels. The colored contours show the probability density function of the clouds of points using a Kernel density estimation (Python scipy.stats.gaussian_kde function provided by SciPy.org). The colors depict the different regions as detailed in the legend of panel (b). (b) Direction of the AR, as defined by the two components of the IVT (see Eq. (1)), at the landing point of the atmospheric river located on the red line displayed on the map in Fig. 3. (c) Mean daily precipitation of the extreme events associated with ARs at all stations for each region and each IVT direction (dots). The vertical lines show ± one standard deviation around the mean. The color code is the same as in panel (b). (For interpretation of the references to color in this figure legend, the reader is referred to the Web version of this article.)

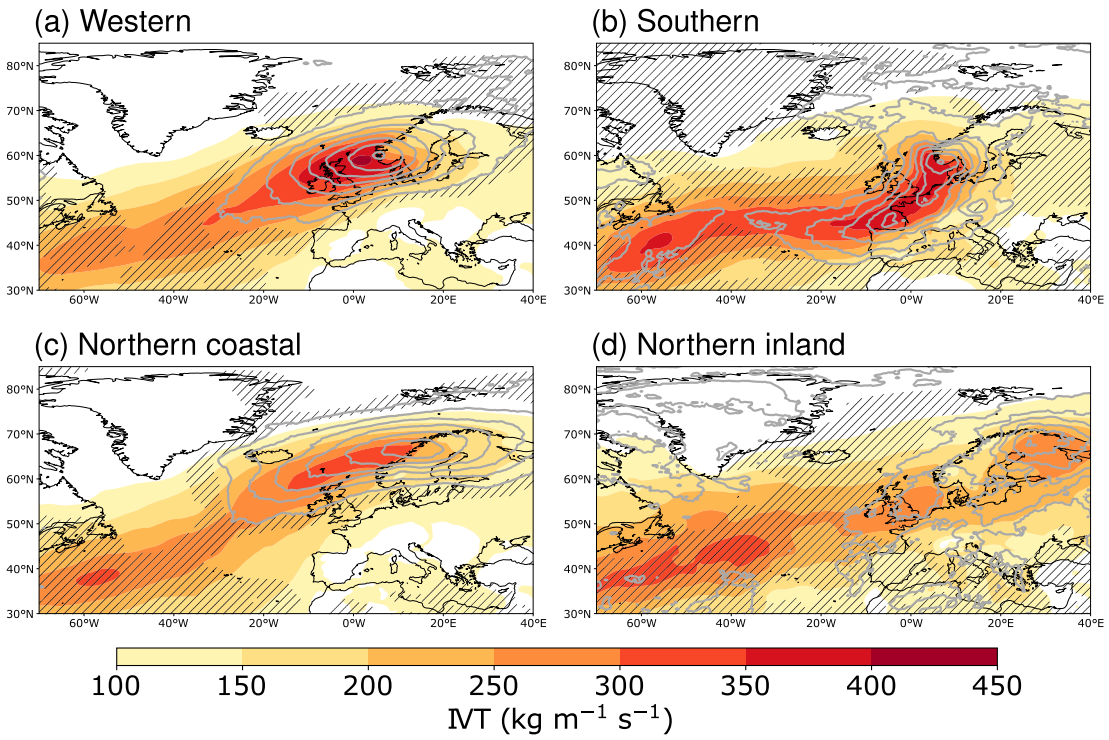

Fig. 6. Composites of the IVT (shading, black stippling when not significant to the 99% level) and AR density (light gray contours, first contour: 30% of time, interval: 10%) over the times with extreme events associated with ARs for four Norwegian regions. The AR density is obtained by averaging binary fields where 0 (1) denotes IVT $<$ ($\geq$) 75th percentile of IVT.

timesteps being given in Table 3. Only four contrasted regions (Western, Southern, Northern coastal, and Northern Inland) are displayed in the remainder of the paper but the others can be found in the Supplemental Material. Apart from the daily E-OBS precipitation and RWB fields that are composited over the individual days, all other fields are composited over the 6-hourly timesteps.

ARs reaching Norway can come from many directions, which depend on the landfall region considered. As seen on the IVT composite and AR density (Figs. 6 and S4), ARs hitting the western side of Norway come from the Norwegian Sea and the ones hitting southeastern Norway rather come from the south. The IVT composite shows a straight band of large IVT extending from the North American East Coast towards Norway for ARs landfalling over western Norway and a bending approach over north-western Europe for ARs making landfall over southeastern Norway. However, the AR density, obtained using the mask as detailed in Sect. 2.2, exhibits highest values closer to Norway, since they all have to reach the Norwegian coast, suggesting that the large IVT over the western part of the North Atlantic is a climatological signal because of the frequent presence of cyclones as well as larger water vapor concentrations due to higher sea surface temperatures there.

Table 3
Number of AR timesteps associated with extreme precipitation events, with the actual number of individual days in parenthesis, and number of cyclones detected within the boxes highlighted in gray on Fig. 8, with the percentage of AR timesteps they represent in parenthesis, for each Norwegian region and the period 1979–2018. NB: not all extreme events are associated with an AR and two regions may share the same AR timesteps.

Region	Number of AR timesteps (individual days)	Number of cyclones detected (percentage)
Western	1284 (533)	1077 (83.9%)
South Western	709 (306)	597 (84.2%)
Middle coastal	1226 (502)	750 (61.2%)
Middle inland	504 (235)	248 (49.2%)
Southern	356 (175)	314 (88.2%)
Eastern	863 (419)	722 (83.7%)
Northern coastal	802 (350)	510 (63.6%)
Northern inland	144 (86)	70 (48.6%)

When making landfall, ARs are associated with larger wind, higher temperatures and of course precipitation. When an AR hits Norway, the precipitation amount is larger than the wet climatology in the region of interest with the extreme events having at least twice the precipitation amount of an average wet day (Figs. 7 and S5) and up to four times the average wet day intensity in the Southern region (Fig. 7b). Not only the region of interest is affected by the precipitation. The events occurring in the Middle coastal and inland regions cause large precipitation amounts over Southwestern Norway as well (Figs. S5c and d). Extreme precipitation in the Southern and Eastern regions affects the whole Southern Norway along with parts of Sweden and Denmark and to a lesser extent the British Isles, France, Benelux and northern Germany (Fig. 7b and S5e,f). The extreme events in the Northern inland region have impacts over large parts of Northern Sweden and Finland (Fig. 7d). The low-level wind strengthens and the 850-hPa temperature increases by more than 1°C, compared to the climatology, over the whole Norway except for the Southern and Northern inland cases, where the former does not exhibit such higher temperatures and the latter stronger winds (see red and blue contours in Figs. 7 and S5).

In agreement with previous studies (e.g., Ralph et al., 2011; Azad and Sorteberg, 2017), ARs are located between a cyclone to the northwest and an anticyclone to the southeast with ARs mainly coming from the southwest (Fig. 5b). Although this pattern is valid for the Western, South Western and Northern inland regions (Fig. 8a,d and S6b), the relative position of the low and high pressure systems can vary and thus the incoming direction of the ARs. In the Southern and Eastern regions, the highest anticyclonic anomaly is located to the east of the cyclone and a lower anticyclonic anomaly is present to the southwest (Figs. 8b and S6f), leading to ARs coming from the south (Fig. 5b). In the Middle

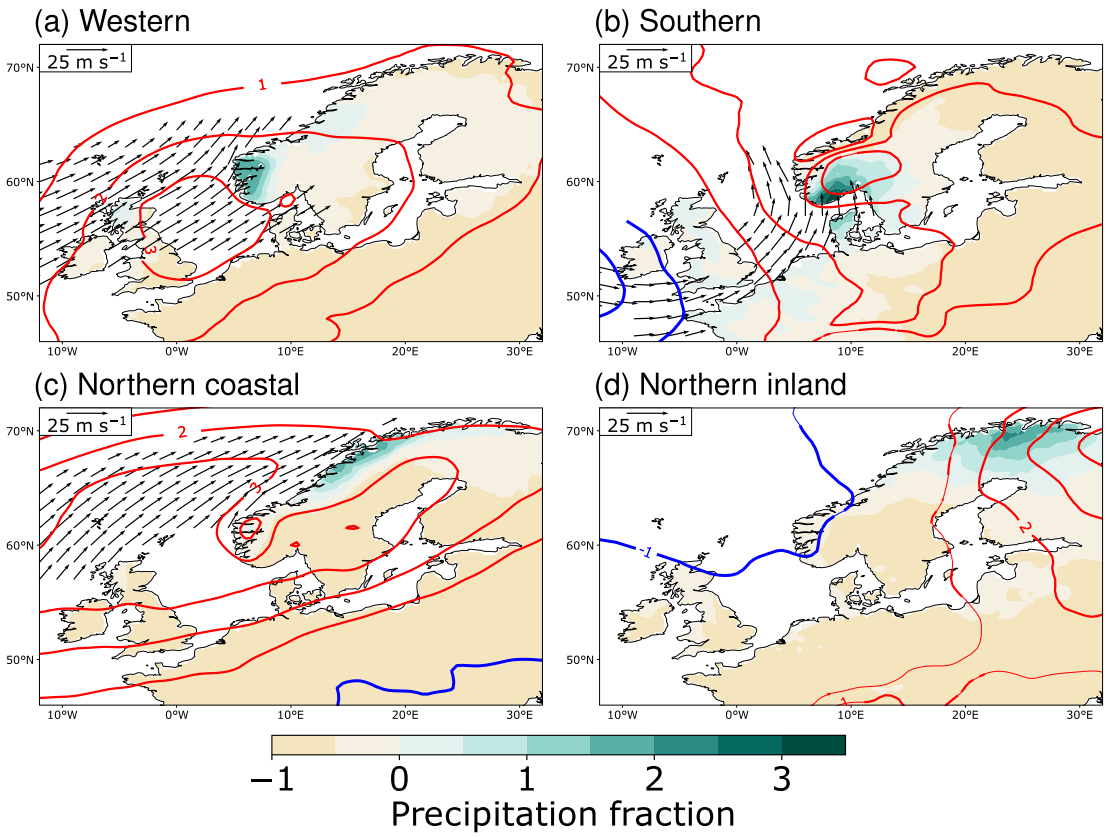

Fig. 7. Composites of the 850-hPa temperature anomalies (red and blue contours for positive and negative anomalies, interval: 1 K, zero-contour omitted, thicker contours for significant values to the 99% level), the fraction of mean wet-day precipitation attributed to the extreme events associated with an AR (shading, see details in the text for its interpretation) and the 950-hPa wind (arrows plotted every third grid point when significant to the 99% level and greater than 15 m s^{-1}) over the times with extreme events associated with ARs for four Norwegian regions. (For interpretation of the references to color in this figure legend, the reader is referred to the Web version of this article.)

coastal and inland and Northern coastal regions, the cyclonic anomaly is located directly to the north of the anticyclonic anomaly (Figs. S6c,d,g) with ARs reaching Norway from the west (Fig. 5b). These different patterns of geopotential anomalies and jets also make the large-scale atmospheric circulation over Europe very different. It can be noted that especially for the Western, Middle and Northern coastal regions, the jet direction is more zonal than the low-level wind (compare arrows in Figs. 7 and S5 with black contours in Figs. 8 and S6). According to Uvo (2003), the extreme precipitation events in southeastern Norway are linked to southerlies whereas westerlies dominate for southwestern Norway (compare Figs. S5a and b with e,f and Figs. S6a and b with e,f).

ARs are often associated with cyclones whose preferred location is tightly linked to the position of the AR itself but overall located to the northwest of the AR (blue contours in Figs. 8 and S6 and e.g. Zhang et al., 2019). An exception is the Northern inland region for which cyclones are most frequent above the region but also to its west (Fig. 8d). The positive anomalies of temperature seen in Figs. 7 and S5 are probably the signature of the cyclones warm sector and the low-level wind may be related to the low-level jet within the AR, ahead of the cold front (see e.g. schematic in Ralph et al., 2018). Except for Middle coastal, inland and Northern coastal regions, the cyclone density maximum is located to the east of the minimum geopotential anomalies suggesting that baroclinic instability takes place and cyclones can still intensify (compare the blue contours to the blue shading in Figs. 8 and S6 and see also the cyclone-centered composites in Figs. 11 and S9).

The type and frequency of Rossby wave breakings associated with the cyclones depend on the location of the cyclones/ARs (Figs. 9 and S7). For the Western, South Western, Middle and Northern coastal and Middle inland regions, anticyclonic wave breaking (AWB) is most frequent and the jet is stronger to the north (Fig. 9, S7 and 8, S6). The presence of AWB is also noticeable from the anticyclonic reversal of the isentropes on the 2-pvu surface (shading in Fig. 9a,c and S7b,c,d). For the Southern and Eastern regions, cyclonic wave breaking (CWB) is most frequent and the jet stronger to the south directed over Western Europe and diverted north towards Norway. The CWB imprint on the 2-pvu surface is marked by a trough over the British Isles followed with a ridge to the east (see shading in Figs. 9b and S7f). These results are consistent with Sodemann and Stohl (2013) who showed that ARs related to AWB exhibit a meridional jet deviated to the north whereas the jet is more zonal when linked to CWB. For the Northern inland region, CWB is most frequent and the upper-level jet is very weak.

The extreme precipitation events associated with ARs are more likely to be associated with cyclone clustering when they occur in the coastal regions (Western, South Western, Middle and Northern coastal) than in other regions of Norway (see contours in Figs. 10 and S8). Up to 40–45% of the extreme events associated with ARs are linked to cyclones clusters (see total numbers of timesteps in Table 3) over the Norwegian Sea for the Western region (Fig. 10a) but only between 10 and 20% for Northern Inland (Fig. 10d). As shown in Figs. 9 and S7, the coastal regions are associated with more frequent AWB over Europe than the more inland regions, which rather exhibit a more localised cyclone density and more frequent CWB. This is in agreement with Sodemann and Stohl (2013) who suggested that the cyclones clusters reaching Norway are associated with AWB whereas single cyclones are rather associated with CWB.

A cyclone-centered analysis is performed for cyclones in the areas of large cyclone density displayed with gray lines in Fig. 8 and whose numbers are specified in Table 3. It reveals that the cyclone intensity distribution is not significantly different among the regions (black

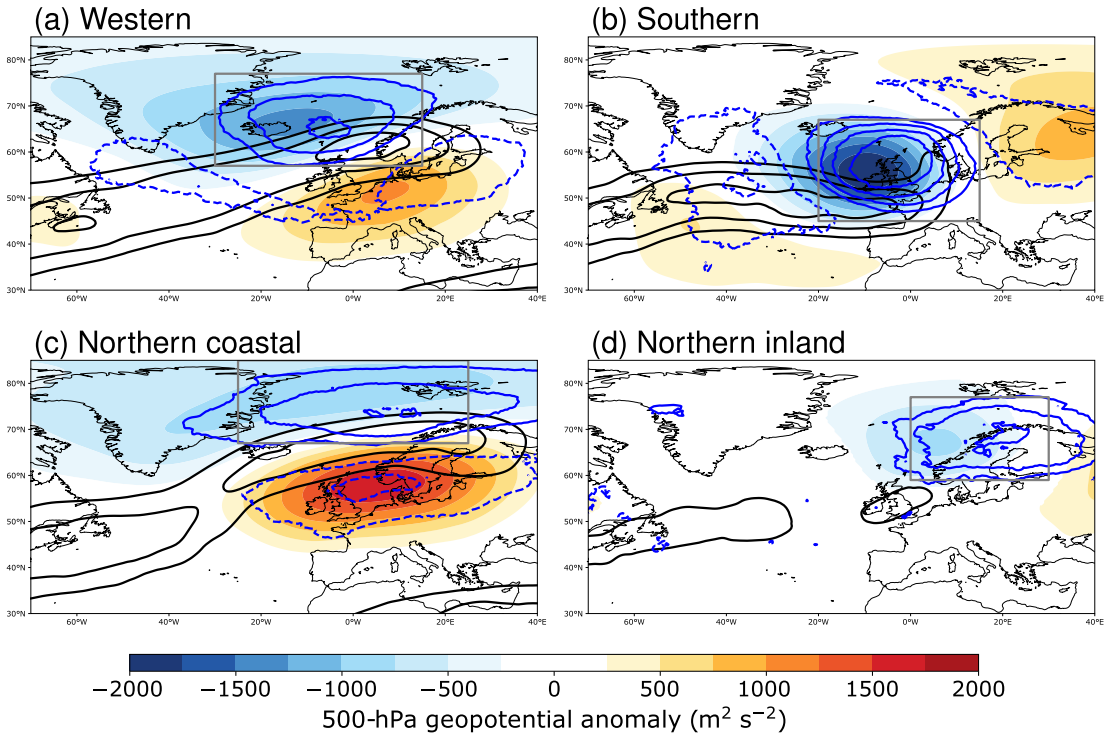

Fig. 8. Composites of the 500-hPa geopotential anomalies (shading only when significant to the 99% level), cyclone density anomalies (blue contours, solid for positive values, dashed for negative values, interval: 10% of the time, zero-contour omitted) and 250-hPa windspeed (black contours, first contour: 30 m s^{-1}, interval: 5 m s^{-1}) over the times with extreme events associated with ARs for four Norwegian regions. The gray box on each panel shows the region in which cyclones' positions are sought when performing the cyclone-centered composites (Fig. 11). (For interpretation of the references to color in this figure legend, the reader is referred to the Web version of this article.)

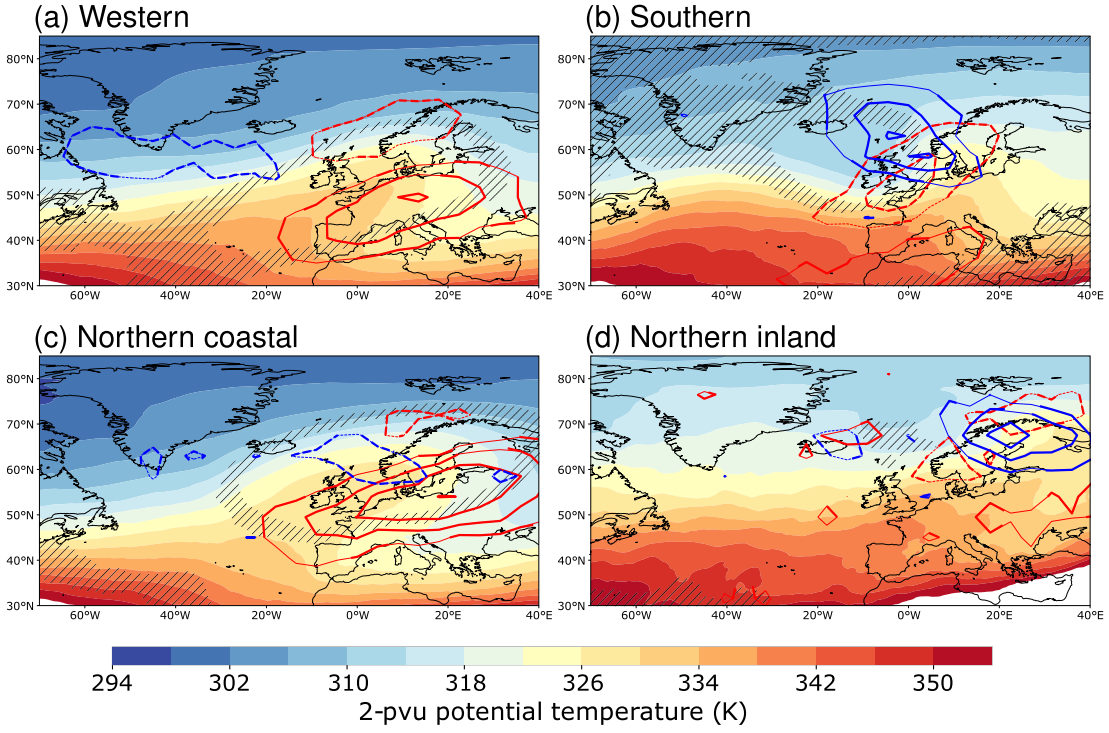

Fig. 9. Composites of the 2-pvu potential temperature (shading, black stippling denotes non-significant areas to the 99% level) and anticyclonic and cyclone wave breaking frequency anomalies (red and blue contours respectively, solid lines for positive values and dashed for negative, thicker lines when significant to the 99% level) over the times with extreme events associated with ARs for four Norwegian regions. (For interpretation of the references to color in this figure legend, the reader is referred to the Web version of this article.)

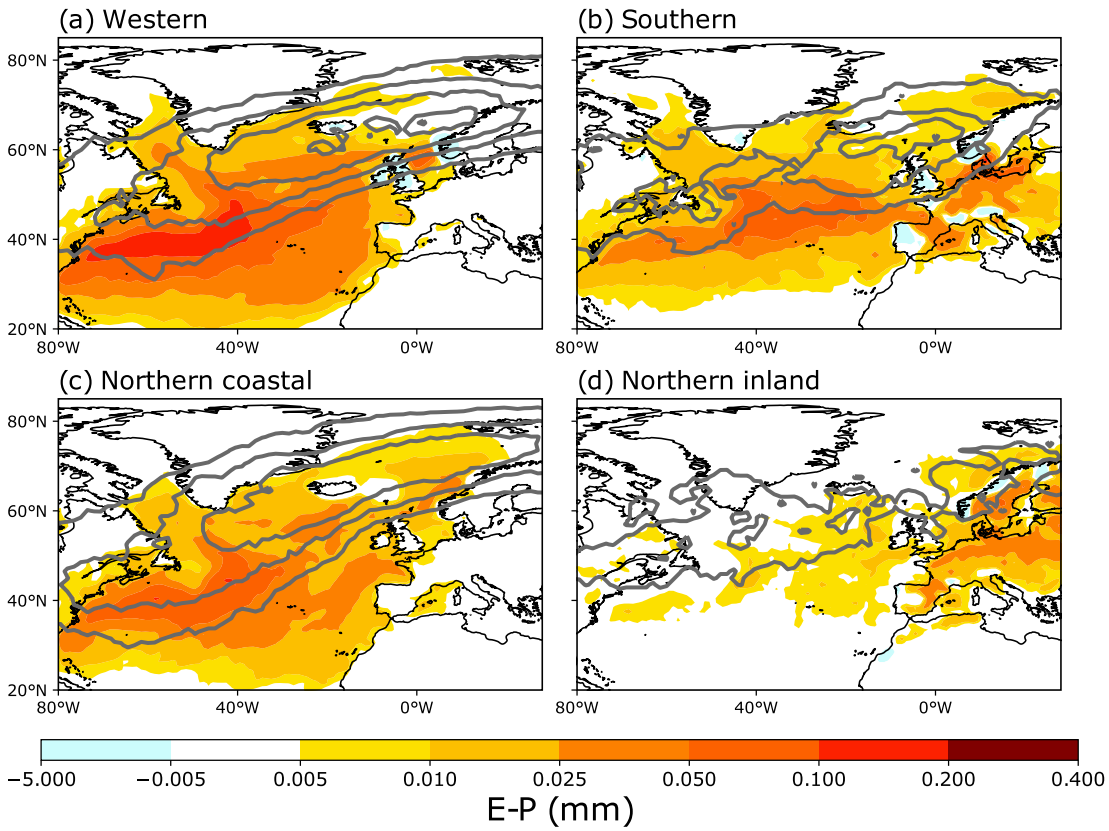

Fig. 10. Cyclone clustering frequency (gray contours, first contour and interval: 10% of the events in Table 3 that are classified as clustered) superimposed to the difference evaporation-precipitation (shading, E-P in mm) within the planetary boundary layer for the air parcels trajectories corresponding to extreme events associated with ARs for the (a) Western, (b) Southern, (c) Northern coastal, and (d) Northern inland regions. The number of starting times or positions are for (a) 2198, (b) 375, (c) 600, and (d) 71.

contours in Fig. 11), whether it be using MSLP or the vorticity at 850 hPa. As in Zhang et al. (2019), ARs are most frequent to the south and southeast of the cyclone centre where the IVT is also largest (shading and purple contours in first row of Fig. 11). According to Fig. 8, the cyclones are located slightly to the east of the upper-level trough meaning that baroclinic instability can still happen and the cyclones intensify (second row in Figs. 11 and S9). Despite not being more intense, cyclones reaching the southern regions seem associated with more precipitation than for the middle and northern regions with warmer temperatures at 850 hPa (third row in Figs. 11 and S9), the precipitation tail to the south following the large IVT and AR frequency (compare with shading and violet contours in first row of Figs. 11 and S9). Note that cyclones over the Northern inland region are the ones with largest precipitation.

Compositing 12-day backwards trajectories shows moisture sources over the North Atlantic for the western coastal regions (Fig. 10a,c and S8b,c) and additional uptake over the continental Europe for the more eastern and inland regions (Fig. 10b,d and S8d,f). The Northern inland region mainly exhibits uptake over continental Europe and negligible moisture uptake over the North Atlantic. The moisture uptake is largest in the Gulf Stream region where the evaporation is climatologically the largest (Marshall and Plumb, 2008), extends west of Europe and up to the region considered. However, it is likely that part of the moisture gathered in the Gulf Stream region has precipitated before reaching the target area. The region of large E-P is also co-located with the position of the starting points of the cyclones' warm conveyor belts (e.g. Eckhardt et al., 2004) and slightly south of the storm track (Hoskins and Hodges, 2002), highlighting the close link between the warm conveyor belts and ARs (Dacre et al., 2019). Note finally that the coastal regions, which feature the strongest extreme precipitation, are also linked with larger moisture uptake compared to the inland regions.

5. Conclusions

We detected ARs that reach Norway in the ERA-Interim reanalysis and linked them to the observed extreme precipitation events over the period 1979–2018. As was shown before, Southwestern Norway is the region where most of the extremes (~78.5%) are associated with ARs. This association happens mainly in fall and early winter when ARs are most frequent (~37% of ARs occur from October to January). More than 50% of the extreme precipitation events occur in summer in the inland regions of Norway and only ~38% of all extremes are associated with ARs. Extreme precipitation associated with ARs contributes to the wet climatology and is associated with an increase in temperature of 1–2°C at 850 hPa due to the passage of the warm front and sector.

Large precipitation amounts do not translate systematically in large IVT or IWV. IWV largely depends on the season with highest (lowest) values in summer (winter) whereas IVT does not seem to be very sensitive to the season. In accordance with the composites of AR density and IVT, the ARs direction when hitting land depends on the region, with a favoured southern direction for the South and Eastern regions and more western direction for the other regions except the far north. Therefore, the amount of precipitation depends on the local conditions, such as the presence or not of topography, the orientation of the topography relative to the incoming atmospheric flow, and the position of the cold front, if present, which may help to force the AR air mass to ascend above the mountains. However, even when the direction of the AR is held constant, the precipitation still varies significantly. This event-to-event variability could be investigated by focusing on one region only.

Apart from the Northern inland region where cyclones associated

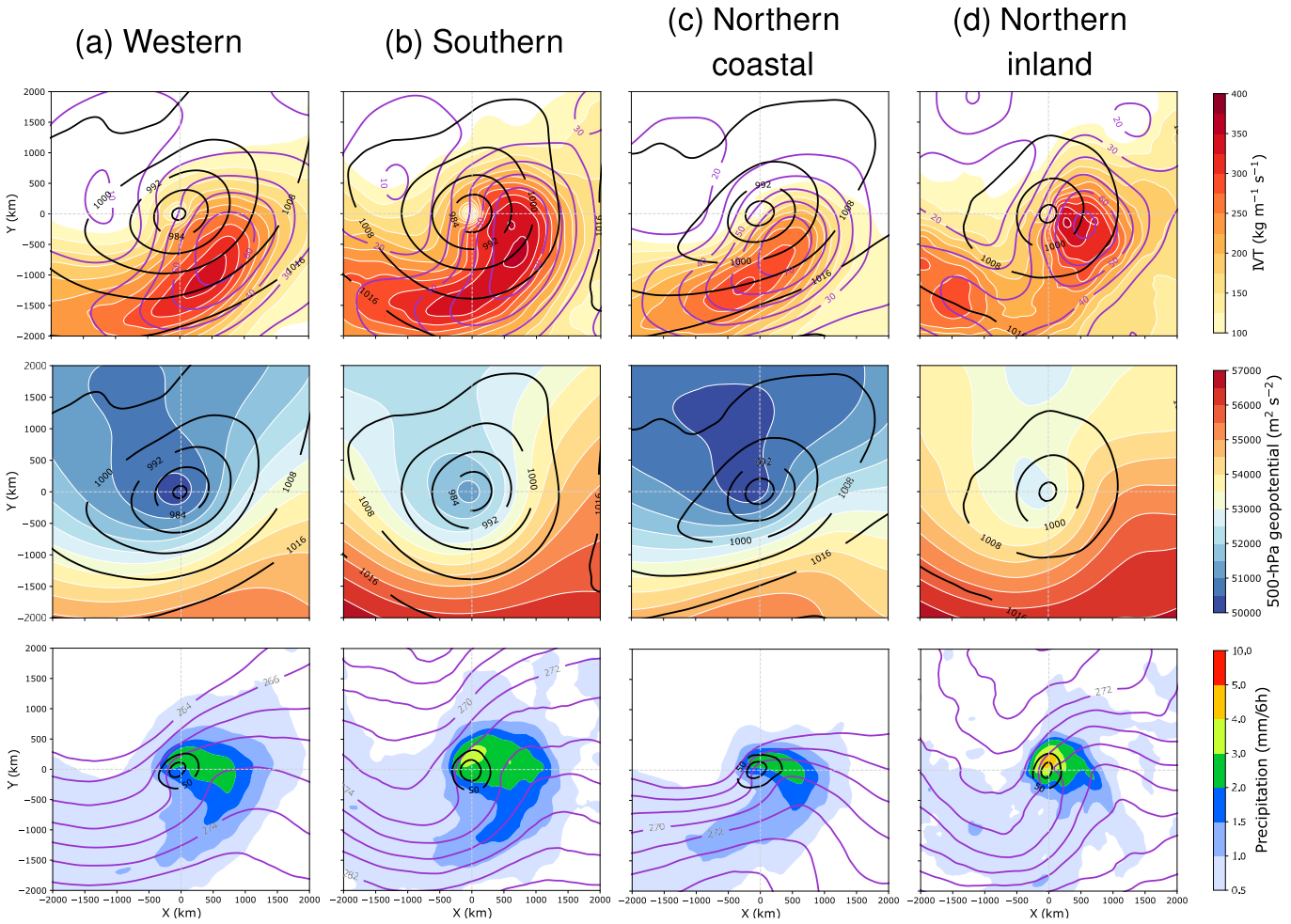

Fig. 11. Cyclone-centered composites for the (a) Western, (b) Southern, (c) Northern coastal, and (d) Northern inland regions. (Top row) MSLP (black contours, interval: 8 hPa), AR density (purple contours, interval: 10% of the time) and IVT (shading, unit: kg m^{-1} s^{-1}). (Middle row) MSLP (black contours, interval: 8 hPa), geopotential at 500 hPa (shading, unit: m^2 s^{-2}). (Bottom row) 850-hPa relative vorticity (black contours, first contour and interval: 50 10^6 s^{-1}), temperature at 850 hPa (purple contours, interval: 2 K from 264 K) and total precipitation (shading, unit: mm per 6h). Cyclones, as defined by local minima of MSLP, are sought in the gray boxes highlighted in Fig. 8. The number and percentages of the time that a cyclone is found in the box are shown in Table 3. (For interpretation of the references to color in this figure legend, the reader is referred to the Web version of this article.)

with ARs are located above the region, the cyclones for the rest of Norway are rather located to the west of Norway over the Nordic seas. ARs reaching Southern and Eastern Norway are associated with cyclonic wave breaking whereas when ARs reach northern or western regions they are associated with anticyclonic wave breaking over Europe as has been observed for the North Pacific (Ryoo et al., 2013; Payne and Magnusdottir, 2014; Hu et al., 2017). Therefore, the Middle coastal, inland and Northern coastal regions are rather dominated by an anticyclonic circulation over Europe when the others are rather dominated by a cyclonic circulation over the Nordic Seas, as also shown in Benedict et al. (2019) for the Northern, Western and Southern regions. However, the Western and South Western regions present a dipole with cyclonic circulation to the north and anticyclonic to the south.

Cyclone-centered composites for each region show that the cyclone intensity is not significantly different among the different regions (whether it be using the MSLP or the relative vorticity at 850 hPa) although the cyclones for the southern regions seem associated with more precipitation than for the middle and northern regions, except the Northern inland region. This precipitation discrepancy may be linked to a larger moisture availability due to larger sea surface temperatures to the south than to the north. It could also be linked to less conducive orientation of the mountain range in Middle Norway (southwest-northeast) to orographically enhanced precipitation as the moist warm air may head more along the mountain range than crossing it. We note that the cyclones can still intensify as baroclinic interaction with the upper levels is still possible. A mesoscale study of the cyclones associated with extreme precipitation events, looking for example at the interaction between front and topography or the role of convection for the summer events, would help understand the similarities and differences found in the present work.

In agreement with previous studies (e.g. Stohl et al., 2008), we find that the moisture source location depends on the season when the extreme event associated with an AR occurs, with more frequent continental sources for summer and the more inland regions of Norway and more frequent ocean sources for fall and winter and the more coastal regions. As the atmospheric moisture content increases with rising global temperatures, it would be interesting to study the eventual changes in moisture sources for future climate scenarios.

Author statement

C. Michel made most of the analysis and wrote the manuscript with comments from all coauthors. A. Sorteberg provided the observational dataset for Norway and guidance at all stages of the study. S. Eckhardt analysed the moisture sources with help of A. Stohl using a method jointly conceived with M. Cassiani. C. Weijenborg provided the cyclone

tracks dataset and performed the cyclone clustering analysis.

Declaration of competing interest

The authors declare that they have no known competing financial interests or personal relationships that could have appeared to influence the work reported in this paper.

Acknowledgements

The authors acknowledge ECMWF for providing the ERA-Interim reanalysis, the Norwegian Meteorological Institute for making the station observations publicly available and the E-OBS dataset from the EU-FP6 project UERRA (https://www.uerra.eu) and the Copernicus Climate Change Service, and the data providers in the ECA&D project (https://eca.knmi.nl). We are grateful to Stephen Outten for sharing the atmospheric river detection code. The authors thank the three reviewers for their comments that improved the manuscript. C. Michel and S. Eckhardt were supported by the NFR KeyClim project (no. 295046).

Appendix A. Supplementary data

Supplementary data to this article can be found online at https://doi.org/10.1016/j.wace.2021.100370.

References

Azad, R., Sorteberg, A., 2017. Extreme daily precipitation in coastal western Norway and the link to atmospheric rivers. J. Geophys. Res. 122, 2080–2095. https://doi.org/10.1002/2016JD025615.

Bao, J.W., Michelson, S.A., Neiman, P.J., Ralph, F.M., Wilczak, J.M., 2006. Interpretation of enhanced integrated water vapor bands associated with extratropical cyclones: their formation and connection to tropical moisture. Mon. Weather Rev. 134, 1063–1080. https://doi.org/10.1175/MWR3123.1.

Benedict, I., Ødemark, K., Npien, T., Moore, R., 2019. Large-scale flow patterns associated with extreme precipitation and atmospheric rivers over Norway. Mon. Weather Rev. 147, 1415–1428. https://doi.org/10.1175/MWR-D-18-0362.1.

Bevacqua, E., Zappa, G., Shepherd, T.G., 2020. Shorter cyclone clusters modulate changes in European wintertime precipitation extremes. Environ. Res. Lett. 15, 124005. https://doi.org/10.1088/1748-9326/abbde7.

Bjerknes, J., Solberg, H., 1921. Meteorological conditions for the formation of rain. Geofys. Publ. 2, 3–61.

Bjerknes, J., Solberg, H., 1922. Life cycle of cyclones and the polar front theory of atmospheric circulation. Geofys. Publ. 3, 1.

Bondevik, S., Aa, A., 2014. Skred utløyst under uvêret Loke 14. november 2005. Technical Report 4/14. Høgskulen i Sogn og Fjordane. https://hvlopen.brage.unit.no/hvlopen-xmlui/bitstream/handle/11250/276491/HiSF_notat_04_14_Bondevik_Aa_jordskred_Loke_2005.pdf?sequence=1&isAllowed=y.

Brands, S., Gutiérrez, J.M., San-Martín, D., 2017. Twentieth-century atmospheric river activity along the west coasts of Europe and North America: algorithm formulation, reanalysis uncertainty and links to atmospheric circulation patterns. Clim. Dynam. 48, 2771–2795. https://doi.org/10.1007/s00382-016-3095-6.

Cornes, R.C., van der Schrier, G., van der Besselaar, E.J.M., Jones, P.D., 2018. An ensemble version of the E-OBS temperature and precipitation datasets. J. Geophys. Res. 123, 9391–9409. https://doi.org/10.1029/2017JD028200.

Dacre, H.F., Clark, P.A., Martinez-Alvarado, O., Stringer, M.A., Lavers, D.A., 2015. How do atmospheric rivers form? Bull. Am. Meteorol. Soc. 1243–1255. https://doi.org/10.1175/BAMS-D-14-00031.1.

Dacre, H.F., Martínez-Alvarado, O., Mbengue, C.O., 2019. Linking atmospheric rivers and warm conveyor belt airflows. J. Hydrometeorol. 20, 1183–1196. https://doi.org/10.1175/JHM-D-18-0175.1.

Dacre, H.F., Pinto, J.G., 2020. Serial clustering of extratropical cyclones: a review of where, when and why it occurs. NPJ Clim. Atmos. Sci. 3 https://doi.org/10.1038/s41612-020-00152-9.

Dee, D.P., Uppala, S.M., Simmons, A.J., Berrisford, P., Poli, P., Kobayashi, S., Andrae, U., Balmaseda, M.A., Balsamo, G., Bauer, P., Bechtold, P., Beljaars, A.C.M., van de Berg, L., Bidlot, J., Bormann, N., Delsol, C., Dragani, R., Fuentes, M., Geer, A.J., Haimberger, L., Healy, S.B., Hersbach, H., Hólm, E.V., Isaksen, L., Kållberg, P., Köhler, M., Matricardi, M., McNally, A.P., Monge-Sanz, B.M., Morcrette, J., Park, B., Peubey, C., de Rosnay, P., Tavolato, C., Thépaut, J., Vitart, F., 2011. The ERA-Interim reanalysis: configuration and performance of the data assimilation system. Quart. J. Roy. Meteor. Soc. 137, 553–597. https://doi.org/10.1002/qj.828.

Eckhardt, S., Stohl, A., Wernli, H., James, P., Fortster, C., Spichtinger, N., 2004. A 15-year climatology of warm conveyor belts. J. Clim. 17, 218–237. https://doi.org/10.1175/1520-0442(2004)017<0218:AYCOWC>2.0.CO;2.

Gao, Y., Lu, J., Leung, L.R., 2016. Uncertainties in projecting future changes in atmospheric rivers and their impacts on heavy precipitation over Europe. J. Clim. 29, 6711–6726. https://doi.org/10.1175/JCLI-D-16-0088.1.

Gimeno, L., Dominguez, F., Nieto, R., Trigo, R., Drumond, A., Reason, C.J.C., Taschetto, A.S., Ramos, A.M., Kumar, R., Marengo, J., 2016. Major mechanisms of atmospheric moisture transport and their role in extreme precipitation events. Atmos. Res. Environ. Resour 41, 117–141. https://doi.org/10.1146/annurev-environ-110615-085558.

Guan, B., Waliser, D.E., Ralph, F.M., Fetzer, E.J., Neiman, P.J., 2016. Hydrometeorological characteristics of rain-on-snow events associated with atmospheric rivers. Geophys. Res. Lett. 43, 2964–2973. https://doi.org/10.1002/2016GL067978.

Guo, Y., Shinoda, T., Guan, B., Waliser, D.E., Chang, E.K.M., 2020. Statistical relationship between atmospheric rivers and extratropical cyclones and anticyclones. J. Clim. 33, 7817–7834. https://doi.org/10.1175/JCLI-D-19-0126.1.

Hanssen-Bauer, I., 2005. Regional Temperature and Precipitation Series for Norway: Analyses of Time-Series Updated to 2004. Technical Report. Norwegian Meteorological Institute, p. 34pp.

Hanssen-Bauer, I., Førland, E.J., 1998. Annual and Seasonal Precipitation Variations in Norway 1896-1997, Klima-Report. Technical Report. Norwegian Meteorological Institute, Oslo, Norway.

Haylock, M.R., Hoftsra, N., Tank, A.M.G.K., Klok, E.J., Jones, P.D., New, M., 2008. A European daily high-resolution gridded data set of surface temperature and precipitation for 1950–2006. J. Geophys. Res. 113, D20119. https://doi.org/10.1029/2008JD010201.

Hecht, C.W., Cordeira, J.M., 2017. Characterizing the influence of atmospheric river orientation and intensity on precipitation distributions over North Coastal California. Geophys. Res. Lett. 44, 9048–9058. https://doi.org/10.1002/2017GL074179.

Heikkilä, U., Sorteberg, A., 2012. Characteristics of autumn-winter extreme precipitation on the Norwegian west coast identified by cluster analysis. Clim. Dynam. 39, 929–939. https://doi.org/10.1007/s00382-011-1277-9.

Hofstra, N., Haylock, M., New, M., Jones, P.D., 2009. Testing E-OBS European high resolution gridded data set of daily precipitation and surface temperature. J. Geophys. Res. 114, D21101. https://doi.org/10.1029/2009JD011799.

Hoskins, B.J., Hodges, K.I., 2002. A new perspective on Northern Hemisphere storm tracks. J. Atmos. Sci. 59, 1041–1061. https://doi.org/10.1175/1520-0469(2002)059<1041:NPOTNH>2.0.CO;2.

Hu, H., Dominguez, F., Wang, Z., Lavers, D.A., Zhang, G., Ralph, F.M., 2017. Linking atmospheric river hydrological impacts on the U.S. West coast to Rossby wave breaking. J. Clim. 30, 2816–2850. https://doi.org/10.1175/JCLI-D-16-0386.1.

Hughes, M., Mahoney, K.M., Neiman, P.J., Moore, B.J., Alexander, M., Ralph, F.M., 2014. The landfall and inland penetration of a flood-producing atmospheric river in Arizona. Part II: sensitivity of modeled precipitation to terrain height and atmospheric river orientation. J. Hydrometeorol. 15, 1954–1974. https://doi.org/10.1175/JHM-D-13-0176.1.

Lavers, D.A., Villarini, G., 2013. The nexus between atmospheric rivers and extreme precipitation across Europe. Geophys. Res. Lett. 40, 3259–3264. https://doi.org/10.1002/grl.50636.

Leung, L.R., Dian, Y., 2009. Atmospheric rivers induced heavy precipitation and flooding in the western U.S. simulated by the WRF regional climate model. Geophys. Res. Lett. 36, L03820. https://doi.org/10.1029/2008GL036445.

Liberato, M.L.R., Ramos, A.M., Trigo, R.M., Trigo, I.F., Durán-Quesada, A.M., Nieto, R., Gimeno, L., 2012. Moisture Sources and Large-Scale Dynamics Associated with a Flash Flood Event. American Geophysical Union (AGU), pp. 111–126. https://doi.org/10.1029/2012GM001244 (chapter 11).

Marshall, J., Plumb, R.A., 2008. Atmosphere, Ocean, and Climate Dynamics: an Introductory Text. Elsevier Academic Press, p. 344.

Martius, O., Schwierz, C., Davies, H., 2007. Breaking waves at the tropopause in the wintertime northern hemisphere: climatological analyses of the orientation and the theoretical LC1/2 classification. J. Atmos. Sci. 64, 2576–2592. https://doi.org/10.1175/JAS3977.1.

McIntyre, M.E., Palmer, T.N., 1983. Breaking planetary waves in the stratosphere. Nature 305, 593–600. https://doi.org/10.1038/305593a0.

Michel, C., Rivière, G., 2011. The link between Rossby wave breakings and weather regime transitions. J. Atmos. Sci. 68, 1730–1748. https://doi.org/10.1175/2011JAS3635.1.

Murray, R.J., Simmonds, I., 1991. A numerical scheme for tracking cyclone centres from digital data. Part I: development and operation of the scheme. Aust. Met. Mag. 39, 155–166.

Neiman, P.J., Shick, L.J., Ralph, F.M., Hughes, M., Wick, G.A., 2011. Flooding in Western Washington: the connection to atmospheric rivers. J. Hydrometeorol. 12, 1337–1358. https://doi.org/10.1175/2011JHM1358.1.

Neiman, P.J., Shick, L.J., Ralph, F.M., Hughes, M., Wick, G.A., 2013. The landfall and inland penetration of a flood-producing atmospheric river in Arizona. Part I: observed synoptic-scale, orographic, and hydrometeorological characteristics. J. Hydrometeorol. 14, 460–484. https://doi.org/10.1175/JHM-D-12-0101.1.

Newell, R., Newell, N., Zhu, Y., Scott, C., 1992. Tropospheric rivers? - a pilot study. Geophys. Res. Lett. 19, 2401–2404. https://doi.org/10.1029/92GL02916.

Outten, S., 2019. Development of an atmospheric river detection algorithm. Technical Report NERSC 10.

Pasquier, J.T., Pfahl, S., Grams, C.M., 2018. Modulation of atmospheric river occurrence and associated precipitation extremes in the North Atlantic region by European weather regimes. Geophys. Res. Lett. 46, 1014–1023. https://doi.org/10.1029/2018GL081194.

Payne, A.E., Magnusdottir, G., 2014. Dynamics of landfalling atmospheric rivers over the North Pacific in 30 years of MERRA reanalysis. J. Clim. 27, 7133–7150. https://doi.org/10.1175/JCLI-D-14-00034.1.

Pisso, I., Sollum, E., Grythe, H., Kristiansen, N.I., Cassiani, M., Eckhardt, S., Arnold, D., Morton, D., Thompson, R.L., Zwaaftink, C.D.G., Evangeliou, N., Sodemann, H., Haimberger, L., Henne, S., Brunner, D., Burkhart, J.F., Fouilloux, A., Brioude, J., Philipp, A., Seibert, P., Stohl, A., 2019. The Lagrangian particle dispersion model FLEXPART version 10.4. Geosci. Model Dev 12, 4955–4997. https://doi.org/10.5194/gmd-12-4955-2019.

Putkonen, J., Roe, G., 2003. Rain-on-snow events impact soil temperatures and affect ungulate survival. Geophys. Res. Lett. 30, 1188. https://doi.org/10.1029/2002GL016326.

Ralph, F.M., Dettinger, M.D., Cairns, M.M., Galarneau, T.J., Eylander, J., 2018. Defining "atmospheric river" how the Glossary of Meteorology helped resolve a debate. Bull. Am. Meteorol. Soc. 4 https://doi.org/10.1175/BAMS-D-17-0157.1, 837–830.

Ralph, F.M., Neiman, P.J., Kiladis, G.N., Weickmann, K., Reynolds, D.W., 2011. A multiscale observational case study of a Pacific atmospheric river exhibiting tropical–extratropical connections and a mesoscale frontal wave. Mon. Weather Rev. 139, 1169–1189. https://doi.org/10.1175/2010MWR3596.1.

Ralph, F.M., Neiman, P.J., Kingsmill, D.E., Persson, P.O.G., White, A.B., Strem, E.T., Andrews, E.D., Antweiler, R.C., 2003. The impact of a prominent rain shadow on flooding in California's Santa Cruz mountains: a CALJET case study and sensitivity to the ENSO cycle. J. Hydrometeorol. 4, 1243–1264. https://doi.org/10.1175/1525-7541(2003)004<1243:TIOAPR>2.0.CO;2.

Ralph, F.M., Neiman, P.J., Rotunno, R., 2005. Dropsonde observations in low-level jets over the Northeastern Pacific Ocean from CALJET-1998 and PACJET-2001: mean vertical-profile and atmospheric-river characteristics. Mon. Weather Rev. 133, 889–910. https://doi.org/10.1175/MWR2896.1.

Ralph, F.M., Neiman, P.J., Wick, G.A., 2004. Satellite and CALJET aircraft observations of atmospheric rivers over the Eastern North Pacific Ocean during the winter of 1997/98. Mon. Weather Rev. 132, 1721–1745. https://doi.org/10.1175/1520-0493(2004)132<1721:SACAOO>2.0.CO;2.

Ralph, F.M., Neiman, P.J., Wick, G.A., Gutman, S.I., Dettinger, M.D., Cayan, D.R., White, A.B., 2006. Flooding on California's Russian River: role of atmospheric rivers. Geophys. Res. Lett. 33, L13801. https://doi.org/10.1029/2006GL026689.

Ralph, F.M., Rutz, J.J., Cordeira, J.M., Dettinger, M.D., Anderson, M., Reynolds, D., Schick, L.J., Smallcomb, C., 2019. A scale to characterize the strength and impacts of atmospheric rivers. Bull. Am. Meteorol. Soc. 100, 269–289. https://doi.org/10.1175/BAMS-D-18-0023.1.

Ramos, A.M., Nieto, R., Tomé, R., Gimeno, L., Trigo, R.M., Liberato, M.L.R., Lavers, D.A., 2016. Atmospheric rivers moisture sources from a Lagrangian perspective. Earth Sys. Dynam 7, 371–384. https://doi.org/10.5194/esd-7-371-2016.

Rivière, G., 2009. Effect of latitudinal variations in low-level baroclinicity on eddy life cycles and upper-tropospheric wave-breaking processes. J. Atmos. Sci. 66, 1569–1592. https://doi.org/10.1175/2008JAS2919.1.

Ryoo, J.M., Kaspi, Y., Waugh, D.W., Kiladis, G.N., Waliser, D.E., Fetzer, E.J., Kim, J., 2013. Impact of Rossby wave breaking on U.S. West Coast winter precipitation during ENSO events. J. Clim. 26, 6360–6382. https://doi.org/10.1175/JCLI-D-12-00297.1.

Sodemann, H., Stohl, A., 2013. Moisture origine and meridional transport in atmospheric rivers and their association with mutliple cyclones. Mon. Weather Rev. 141, 2850–2868. https://doi.org/10.1175/MWR-D-12-00256.1.

Sousa, P.M., Trigo, R.M., Barriopedro, D., Soares, P.M.M., Ramos, A.M., Liberato, M.L.R., 2017. Responses of European precipitation distributions and regimes to different blocking locations. Clim. Dynam. 48, 1141–1160. https://doi.org/10.1007/s00382-016-3132-5.

Stohl, A., Forster, C., Sodemann, H., 2008. Remote sources of water vapor forming precipitation on the Norwegian west coast at 60°N - a tale of hurricanes and an atmospheric river. J. Geophys. Res. 113, D05102. https://doi.org/10.1029/2007JD009006.

Stohl, A., James, P., 2004. A Lagrangian analysis of the atmospheric branch of the global water cycle. Part I: method description, validation, and demonstration for the August 2002 flooding in Central Europe. J. Geophys. Res. 5, 656–678, 1010.1175/1525-7541(2004)005<0656:ALAOTA>2.0.CO;2.

Thorncroft, C.D., Hoskins, B.J., McIntyre, M., 1993. Two paradigms of baroclinic-wave life-cycle behaviour. Quart. J. Roy. Meteor. Soc. 119, 17–55. https://doi.org/10.1002/qj.49711950903.

Trigo, R.M., Varino, F., Ramos, A.M., Valente, M.A., Zêzere, J.L., Vaquero, J.M., Gouveia, C.M., Russo, A., 2014. The record precipitation and flood event in iberia in december 1876: description and synoptic analysis. Front. Earth Sci. 2 https://doi.org/10.3389/feart.2014.00003.

Tsopouridis, L., Spensberger, C., Spengler, T., 2020. Characteristics of cyclones following different pathways in the Gulf Stream region. Quart. J. Roy. Meteor. Soc. 1–16. https://doi.org/10.1002/qj.3924.

Uvo, C.B., 2003. Analysis and regionalization of Northern European winter precipitation based on its relationship with the North Atlantic Oscillation. Int. J. Climatol. 23, 1185–1194. https://doi.org/10.1002/joc.930.

Waliser, D., Guan, B., 2017. Extreme winds and precipitation during landfall of atmospheric rivers. Nat. Geosci. 10, 179–184. https://doi.org/10.1038/NGEO2894.

Weijenborg, C., Spengler, T., 2020. Diabatic heating as a pathway for cyclone clustering encompassing the extreme storm dagmar. Geophys. Res. Lett. 47 https://doi.org/10.1029/2019GL085777.

Whan, K., Sillmann, J., Schaller, N., Haarsma, R., 2020. Future changes in atmospheric rivers and extreme precipitation in Norway. Clim. Dynam. 54, 2071–2084. https://doi.org/10.1007/s00382-019-05099-z.

Zavadoff, B.L., Kirtman, B.P., 2020. Dynamic and thermodynamic modulators of European atmospheric rivers. J. Clim. 33, 4167–4185. https://doi.org/10.1175/JCLI-D-19-0601.1.

Zhang, Z., Ralph, F.M., Wheng, M., 2019. The relationship between extratropical cyclone strength and atmospheric river intensity and position. Geophys. Res. Lett. 46, 1814–1823. https://doi.org/10.1029/2018GL079071.

Zhu, Y., Newell, R., 1998. A proposed algorithm for moisture fluxes from atmospheric rivers. Mon. Weather Rev. 725–735. https://doi.org/10.1175/1520-0493(1998)126<0725:APAFMF>2.0.CO;2.